



Investigation of a highly underexpanded jet with real gas effects confined in a channel: flow field measurements

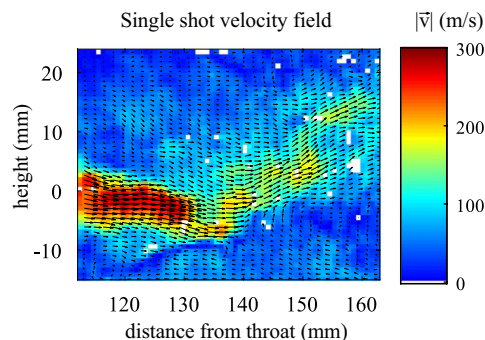
Benoît Fond¹ · Cheng-Nian Xiao² · Christophe T'Joen³ · Ruud Henkes³ · Peter Veenstra³ · Berend G. M. van Wachem¹ · Frank Beyrau¹

Received: 30 May 2018 / Revised: 17 August 2018 / Accepted: 16 September 2018 / Published online: 1 October 2018
© Springer-Verlag GmbH Germany, part of Springer Nature 2018

Abstract

This article describes experiments to investigate the fluid-to-wall interaction downstream of a highly underexpanded jet, with a pressure ratio of 120, confined in a channel. Heat transfer induced by Joule-Thomson cooling, which is a real gas effect in such a configuration, has critical implications on the safety of pressurised gas components. This phenomenon is challenging to model numerically due to the requirement to implement a real gas equation of state, the large range of (subsonic and supersonic) velocities, the high turbulence levels and the near-wall behaviour. An experimental setup with simple geometry and boundary conditions, and with a wide optical access was designed and implemented. It consisted of a high-pressure gas reservoir at controlled temperature and pressure, discharging argon through a nozzle into a square channel. This facility was designed to allow for a steady-state expansion from over 120 bar to atmospheric pressure for over 1 min. The choice of fluid, pressure and temperature regulation system, and the implementation of a high pressure particle seeding system are discussed. The gas dynamics of this flow was then investigated by two separate optical techniques. Schlieren measurements were used to locate the position of the Mach disk, and planar particle image velocimetry (PIV) was used to measure the turbulent velocity field in the regions of lower velocity downstream. Mie scattering images also indicated the presence of a condensed argon phase in the supersonic region as expected from previous studies on nucleation. The observed location of the sharp interface at the Mach disk was found to be in excellent agreement with the Crist correlation. Rapid statistics were derived from the PIV measurements at 3 kHz. The recirculation zone was found to extend about 4 channel heights downstream, and in the region between 2 and 3 channel heights downstream, a continuous deceleration on the centerline velocity was observed in line with the narrowing of the recirculation zone. The first and second velocity moments as well as Reynold stresses were quantified, including pdf distributions. In addition, a sensitivity and repeatability analysis, an evaluation of the PIV random uncertainty, as well as an estimation of errors induced by particle inertia were performed to allow for a full quantitative comparison with numerical simulations.

Graphical abstract



1 Introduction

Expansion cooling (or heating) in choked flows is an important thermodynamic phenomenon. In many industrial devices, e.g. in pressure regulators or across choke valves, fluids are expanded from a high pressure to a moderate or atmospheric pressure. Due to the Joule–Thomson effect in real gases, this expansion can be associated with a significant change in the fluid stagnation temperature. As an example, expanding methane adiabatically from 200 bar and 20 °C to atmospheric pressure results in a temperature of -68 °C. At such temperatures, many metallic alloys as well as elastomers exhibit brittle behaviour, with potential catastrophic effects. In these conditions, the material may suddenly fail when exposed to a high stress (e.g. due to pressure, impact or thermal stress). This can lead to a loss of containment or a full bore rupture in the context of gas pipelines, or localised gas leakages which may result in jet fires ultimately compromising whole facilities. Thermal stresses at low temperatures were responsible for the well-documented Longford accident, where the loss of containment led to a deflagration which claimed two lives and injured eight persons in Australia (Dawson and Books 1999). Understanding the material temperature during a significant transient event, such as a depressurisation, is therefore vital to ensure safe operation. The fluid to wall heat transfer, the thermal properties and the duration of the heat transfer dictate the temperature reached by the materials. The internal geometry of the pressure regulator or valve consists of a narrow flow passage followed by a larger channel, which serves to control or set the flow rate/pressure. A pressure ratio (PR) of over 100 is frequently encountered. Upon leaving this narrow passage, the fluid flow undergoes a transition between a supersonic highly underexpanded “free” jet to a subsonic fully developed turbulent channel flow as illustrated by the schematic of Fig. 1. Predicting the fluid to wall heat transfer under such conditions necessitates a highly advanced computational fluid dynamics (CFD) model for compressible flow with non-ideal gases, capable of simultaneously capturing the supersonic

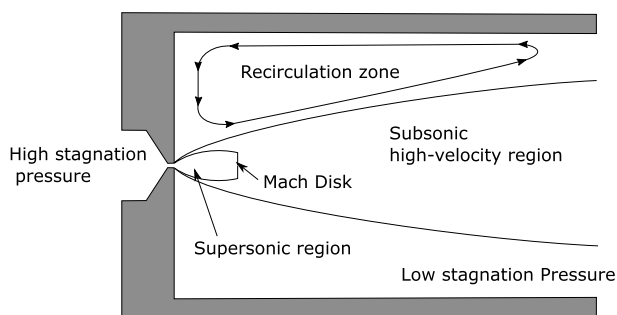


Fig. 1 Schematic of a high pressure expansion in a channel

region, the subsonic turbulent jet, as well as the boundary layer. This is undoubtedly a significant challenge. The validation of such numerical modelling effort is highly reliant on the availability of accurate and comprehensive data sets obtained in well-defined experiments.

There is a large body of literature on experimental investigations of underexpanded jets. Many studies have focused on the compressible features of free jets, mostly using Schlieren imaging as in the seminal article by Crist and co-workers in 1966 (Crist et al. 1966), or later using advanced laser techniques to measure temperature, velocity, pressure and recently the speed of sound (Paul et al. 1989; Naik et al. 2009; Förster et al. 2018). From a heat transfer standpoint, measurements of fluid-to-wall heat transfer rates were reported on underexpanded jets impinging on plane (Rahimi et al. 2003) or cylindrical surfaces (Vinze et al. 2017). In confined configurations, such as in the case of an underexpanded jet issuing into a channel, there are only few experimental (Meier et al. 1980; Hwang et al. 1993) or numerical studies (Lijo et al. 2012; Arun Kumar and Rajesh 2017), and they are focused on the description of the compressible features of the flow. No quantitative measurements of the velocity or temperature fields in such configurations were performed to date. Heat transfer studies of confined jets in channels were limited to the transitional region of low velocity subsonic flows downstream of sudden expansions (Krall and Sparrow 1966; Baughn et al. 1984). To our knowledge, no studies have investigated the fluid to wall heat transfer characteristics of underexpanded jet transitions in channels.

Since predicting the fluid to wall heat transfer is the ultimate goal for the low temperature design of materials in industrial jet expansion applications, one may question whether it is strictly necessary to measure fluid quantities, which is experimentally complex and expensive or whether measuring heat transfer rates, for example from relatively simple wall temperature measurements may be sufficient. Heat transfer rates derived from simulations or experiments are both associated with high uncertainty. In addition, a comparison of heat transfer rates alone does not guarantee that the flow physics are accurately captured. The availability of fluid data, such as temperature, pressure, density or velocity, is therefore required for the validation of the CFD model.

For the considered compressible flow, which is associated with significant heat transfer and real gas effects, quantities of particular interest are: (1) the velocity field, which describes the turbulent flow and (2) the temperature field, which reveals real gas compressible effects, scalar mixing, and is ultimately the driver for heat transfer. Obtaining temperature and velocity simultaneously would have the additional advantage of providing access to the products of the temperature and velocity fluctuations (Schreibvogel et al. 2016). After averaging, these represent the turbulent

diffusion terms, which are at the cornerstone of several CFD models. Once the simulations have attained the adequate level of refinement, such that agreement in the flow quantities is reached, the accuracy of the near-wall model can be tested by comparison with fluid-to-wall heat transfer rate measurements, derived for example from wall temperature measurements. The present article focuses on the first step of this validation effort, which is the design and implementation of the flow and the characterisation of the flow field using laser diagnostics. In the future, fluid temperature measurements, as well as fluid-to-wall heat transfer rate measurements will complement the flow field measurements.

The transitional nature of the flow as illustrated in Fig. 1 calls for a thorough analysis of the diagnostic options for the flow field measurements. Optical measurements are well suited for the observation of turbulent flows, offering high spatial and temporal resolution, while being only weakly intrusive. Underexpanded jets have often been studied by Schlieren or shadowgraphy techniques (Crist et al. 1966). Those techniques are experimentally simple and yield a two-dimensional image of the spatial derivative along one direction of the density field but they have the limitation of being line-of-sight averaged. They are, however, well suited to measure the location and diameter of the Mach disk in highly underexpanded jets. To avoid line-of-sight averaging, planar laser-induced fluorescence of acetone (Yu et al. 2013) or NO molecules (Wilkes Inman et al. 2008) was also used, in which the fluorescent molecules are added to the stream to visualise the density field.

For measuring the velocity, three main categories of optical techniques can be considered: particle-based techniques, molecular Doppler effect-based techniques, and molecular tagging techniques. Particle-based techniques, such as Particle Image Velocimetry (PIV), Laser Doppler Velocimetry (LDV) or Doppler Global Velocimetry (DGV) use particles as tracers for the flow velocity. While those approaches can provide one-, two- or even three-dimensional measurements of up to all three components of velocity with high spatial (Pfadler et al. 2009; Scarano 2013) and temporal resolution (Abram et al. 2013), which are very comprehensive datasets, they rely on the particle motion following the flow velocity. In the regions of sudden acceleration or deceleration, such as across shocks, stringent requirements are imposed on the choice of particles in terms of a high drag and low particle inertia to maintain a low slip velocity. 500 nm oil droplets were used in combination with laser Doppler velocimetry in a sonic jet (Chuech et al. 1989). 2 μm porous particles (with a density between 0.2 and 2 g/cm^3) were used for Particle Image Velocimetry in an underexpanded jet with a PR of 20 (Yüceil 2017). 10-nm oxide particles (Al_2O_3 and SiO_2 with a density of 2 g/cm^3) were seeded in a supersonic jet ($M = 6$) at the outlet of a combustion chamber (Chauveau et al. 2006). The response of similar nanometer-size

oxide particles was also characterised across a stationary oblique shock, and response times on the order of 1 – 3 μs were reported (Ragni et al. 2011). Interestingly, ice clusters which formed from moist air under the low static temperature conditions of the highly supersonic region or condensing droplets from acetone were also used for velocimetry with an estimated size of a few nanometres (Clancy and Samimy 1997).

To avoid issues related to particle seeding, such as the deposition or contamination of flow elements and particle-flow slip, gaseous molecules can also be probed for velocimetry. In the planar laser-induced fluorescence approach, also called PLIF, the Doppler shift in the absorption line of NO molecules seeded into the flow is probed using various methods such as scanning the laser wavelength (Naik et al. 2009), using a broadband source (Paul et al. 1989), or a two line approach (McMillin et al. 1993). The filtered Rayleigh scattering technique, which is also based on the Doppler shift, uses the scattered light from the constituent molecules of the gas, and therefore does not require gaseous seeding (Forkey et al. 1996). These approaches also permit the simultaneous measurements of the density and temperature, but they are limited to high velocity flows, in which the Doppler effect can be accurately captured and therefore they would not be well suited to image boundary layers or recirculation zones in a confined flow. Finally, molecular tagging techniques typically use a write and probe concept. A line is written by one laser either by dissociating a molecule or exciting it into a long-lived state, which can be subsequently probed by laser-induced fluorescence with a second laser (Miles et al. 1989). The velocity is derived from observing the location of a point, a line or an array of lines which has been advected from the writing location. The relatively recent advent of high power density femtosecond lasers allowed for simpler approaches with a single laser such as FLEET (Michael et al. 2011; Burns and Danehy 2017; DeLuca et al. 2017). This is a powerful concept for large high speed flow facilities, e.g. at NASA, which can also yield the flow acceleration, yet it has a measurement spacing and/or spatial resolution on the order of several millimeters, which is unsuitable for the description of the targeted turbulent channel flow.

The challenge in the transitional flow of interest from both a numerical and experimental standpoint lies in the wide range of velocities and spatial scales. The high pressure ratio results in highly supersonic velocities ($M > 5$ for PR > 100) while the heat transfer is mainly influenced by relatively low velocity turbulent regions in the vicinity of the wall. While molecular velocimetry approaches would be well suited to derive the high velocity features of the underexpanded jet, those techniques would offer a lower spatial resolution and accuracy than particle image velocimetry for

the investigation of the turbulent flow field in the subsonic regions.

In this study, planar velocity measurements were performed in the subsonic regions at kHz-rate using particle image velocimetry of solid-seeded particles. To overcome the limitations of PIV in supersonic and transonic regions, it is complemented with Schlieren imaging which is performed non-simultaneously to visualise the location and the size of the Mach disk in the transonic region. The combination of those two techniques permits to address the wide range of velocities in this flow with a limited experiment complexity.

1.1 Roadmap through the paper

This article focuses on the design and implementation of the flow test case and on the characterisation of the flow gas dynamics. The test case consists of a nozzle which sustains a continuous expansion from 120 to 1 bar into a square section for an extended duration of over a minute. The design of the facility is described in Sect. 2, with focus on the choice of fluid, the pressure and temperature regulation, and the implementation of a high-pressure particle seeding system. The implementation of the optical measurements, both Schlieren imaging and PIV is then discussed in Sect. 3. Schlieren measurements of the underexpanded jet structures, e.g. the Mach disk are presented in Sect. 4.1. The results of kHz-rate particle image velocimetry are extensively analysed in Sect. 4.2 and first and second order statistics derived. Finally, in order to enable the quantitative comparison with the results of numerical simulation, in Sect. 4.3, a sensitivity analysis based on convergence, size of interrogation area, and repeatability is performed together with an evaluation of the random PIV uncertainty and of errors related to particle tracing.

2 Experimental facility

2.1 Design criteria

This study aims at developing predictive capabilities for the heat transfer downstream of a choked flow, using a canonical experiment to reveal the effects encountered in real gas piping components. A suitable experiment should have a pressure ratio across the expansion which is high enough to reveal real gas effects representative of typical choke valve conditions, and run long enough and with a sufficient large temperature difference between the fluid and the wall to allow for accurate heat transfer measurements. Also the inlet conditions and geometry should be steady and well described for the validation of the numerical models.

In the simplest configuration, the channel downstream of the throat ends into the ambient (being the local exhaust gas

ventilation inside the laboratory), which results in a near-atmospheric back pressure. The inlet pressure controls the pressure ratio, and can be adjusted by means of a pressure reducing regulator placed between the pressurised gas reservoir and the throat.

2.2 Fluid supply

The choice of gas plays an important role, since it determines the maximum pressure at which the test gas can be supplied, as well as the cooling (or heating) induced by the Joule–Thomson effect. Various gas cylinders were considered. To estimate the stagnation temperature of the stream downstream of the expansion, one can simulate an adiabatic expansion from the cylinder pressure to the channel pressure, i.e. 1 bar. Isenthalpic lines are drawn for each gas which crosses the initial cylinder pressure (based on available industrial gas cylinders) and the ambient temperature in Fig. 2. For example, an isenthalpic expansion from a 230-bar oxygen cylinder at 293 K to atmospheric pressure is equivalent to following the oxygen line from right to left starting at 230 bar and 293 K and ending at 1 bar and about 240 K. As observed, expanding methane from 230 bar produces the lowest temperature (198.5 K). However, to avoid releasing flammable gases, methane is not considered for this experiment. Argon and carbon dioxide with temperatures after expansion of 206.9 K and 207.6 K, respectively, would in principle both be safe and economical alternatives, since they are abundant and inert gases. As higher pressures would allow expansions of higher pressure ratios, which are associated with stronger compressibility effects relevant to the industrial applications and more challenging for the models, argon cylinders at 300 bar were chosen as the fluid supply.

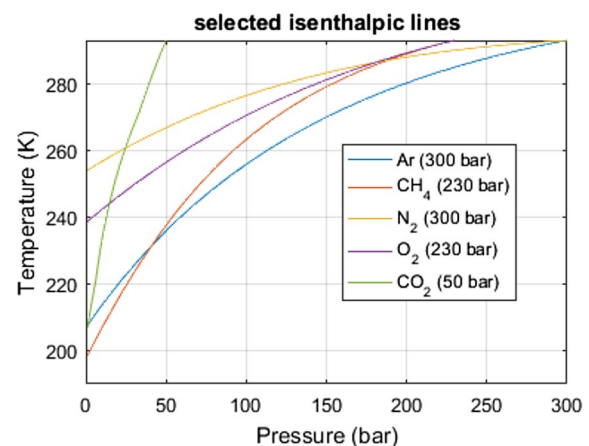


Fig. 2 Selected isenthalpic lines for argon, methane, nitrogen, oxygen and carbon dioxide, intersecting 293 K and the respective initial cylinder pressures

The selected argon cylinder (BOC #11-ZN, Argon Pureshield) contains a mass of 14 normal cubic meters (Nm^3) of argon with 99.998% purity. Impurities are typically O_2 (2 vpm or volume per million), N_2 (5 vpm), CO_2 (1 vpm), CO (1 vpm), H_2 (1 vpm), hydrocarbons (1 vpm) and moisture according to analysis of samples by the supplier.

The pressure was regulated by a single-stage pressure reducing regulator (Conoflow HP300B15N61PABJ) with a range of outlet pressures from 30 to 176 bar. The so-called “flow curves” provided by the manufacturer express the ability of the pressure regulator in maintaining a constant pressure at the outlet for varying flow rate or upstream pressure. At a mass flow rate of $4 \text{ Nm}^3/\text{min}$, an outlet pressure initially at 120 bar will be maintained within 5 bar while the cylinder pressure drops from 300 to 200 bar. Together with the large cylinder volume, this provides a stable supply of high pressure fluid over a long test duration ($> 1 \text{ min}$) at such high flow rates. A one-minute duration would allow sufficient cold penetration in the sidewall materials for accurate heat transfer rate measurements, based on a first pass thermal assessment.

The throat diameter was chosen to be 1.55 mm so that for argon at an upstream pressure of 120, the throat mass flux ($2.5 \text{ Nm}^3/\text{min}$) is within the regulator capabilities. The throat geometry consisted of a converging nozzle starting from 6.9 mm at a contraction angle of 118° followed by a 5-mm-long constant area section with a diameter of 1.5 mm. Upon flowing through the nozzle, the fluid is released into the centre of a square channel with an internal height 50 mm and a length of 500 mm. The Reynolds number considering the height of the test section and the mass flow rate would be approx. 75,000 under fully developed conditions, which ensures sufficiently high turbulence levels that are representative of gas expansion phenomena found in full scale industrial pipelines.

2.3 High pressure particle seeder

To perform velocity measurements with particle image velocimetry, tracer particles must be introduced into the flow upstream of the expansion, where the fluid pressure is 120 bar. For this purpose, a high pressure particle seeder was designed and incorporated in the fluid supply. The seeder consists of a pressure vessel (Newport Scientific Inc.) with an internal volume of 0.85 l for an inner diameter of 65 mm and an inner length of 254 mm, and a pressure rating of 625 bar. Using an internal structure, fastened to the vessel head, the internal volume was divided into two plenums separated by a sintered plate, as in traditional fluidised bed seeder designs. The flow enters a first 0.1-l plenum covered by a 5-mm-thick brass-sintered plate (Tridelta Siperm B12) above which there is powder which was filled to a height of approximately 5 cm. A critical parameter in the operation of

fluidised bed seeder is the fluid velocity in the top plenum. Low pressure ($< 10 \text{ bar}$) fluidised bed seeders were found to provide steady particle number densities (or seeding densities) in the range 5×10^{10} – 5×10^{11} particles per m^3 , which is suitable for PIV, at flow rates corresponding to a velocity in the top plenum on the order of 0.1 m/s. The inner diameter of the vessel of 65 mm was therefore chosen to achieve such velocity during the rig operation. The effect of the pressure on the particle entrainment is not yet clear since it depends on the flow regime of the particle entrainment: there is a weak influence via the dynamic viscosity in the Stokes regime ($Re_p < 1$), where the drag force is

$$F_D = 3\pi\mu d_p v, \quad (1)$$

but a far stronger effect via the density at higher slip velocities in the transition drag regime ($Re_p > 1$), where the drag force is

$$F_D = \frac{1}{2}\rho v^2 \frac{d_p^2 \pi}{4} C_D, \quad (2)$$

with $C_D = 18.5Re_p^{-0.6}$. In these expressions, μ is the fluid dynamic viscosity, d_p is the particle diameter, v is the particle-fluid slip velocity, ρ is the fluid density, and C_D is the drag coefficient, expressed as a function of the particle Reynolds number $Re_p = \frac{\rho v d_p}{\mu}$. Note that for argon at 120 bar, and

considering a 1- μm sphere, the particle Reynolds number is 15 at a slip velocity of 0.1 m/s, which is outside the Stokes regime. By designing for a similar fluid velocity in the second plenum, it is anticipated that the higher density will increase the seeding density with respect to the low pressure seeders as to compensate for the decrease in the gas density, hence in particle number densities across the expansion. The described particle seeder was found to provide particle seeding densities in the order of 1×10^{11} – 4×10^{11} particles/ m^3 downstream of the 120 to 1 bar expansion, which was adequate for this experiment.

2.4 Pressure and temperature control

The lines, actuators and sensors used to control the expansion are shown in Fig. 3. The main function of the system was to continuously supply argon at a steady pressure of 120 bar from a 300-bar pressurised gas cylinder by means of the pressure reducing regulator mentioned above. Before starting an experiment, all three solenoid valves were closed, and the pressure upstream of the valve was manually set under a no-flow condition using the pressure regulator. The pressure was set at approximately 135 bar to account for the drop in the outlet pressure with increasing mass flow rates as specified by the manufacturer’s “flow curves”, referred to as the “droop” effect. At start-up, the solenoid valve represented

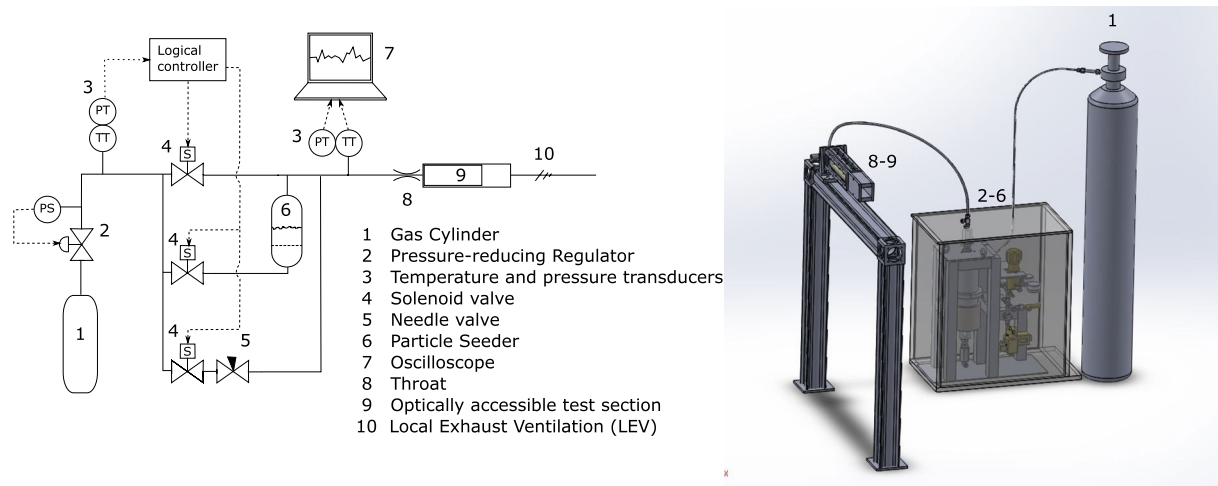


Fig. 3 Simplified flow diagram (left) and isometric view (right) of the gas supply system

at the top in Fig. 3 was opened, and the throat became the smallest restriction in the system. This is where the choked condition was eventually reached, resulting in a pressure of 120 bar directly upstream of the nozzle, considering that the head losses in the piping and valves are negligible. Due to the large volume of the vessel, it took approximately 2 s to establish a steady state pressure of 120 bar upstream of the throat. Once the steady state pressure was reached, the valve upstream of the seeder was opened and the main valve was closed. An additional line, bypassing the seeder, allowed for the independent control of the seeding level by adjusting the pressure drop using a needle valve as represented in the lower branch in Fig. 3.

The critical safety aspect of this experiment was the presence of low temperatures at which steel and elastomers may exhibit brittle behaviour. Normal operation with an outlet pressure of 120 bar resulted in a temperature of 260 K at the pressure regulator outlet as expected from the argon isenthalpic line in Fig. 2. On the other end, unintended operation with a set regulator pressure of 1 bar would result in a temperature below 210 K. High-pressure solenoid valves with seat materials rated to such low temperature levels could not be procured. Instead, the components used were all rated to a minimum service temperature of 243 K or lower and a logical control based on the signal of a pressure transducer prevented the valve from opening in case of a low regulator set pressure. Thermocouple-based control was also added for redundancy. In addition to prevent ice clusters from moist air to form blockages in the supply lines, the system was purged with a flow of dry nitrogen prior to operation. The purging lines are not included in Fig. 3. A safety pressure-relief valve (Seetru 3294) with a relief pressure of 198 bar was also installed downstream of the pressure regulator (also not shown) and routed to the local exhaust ventilation to prevent over pressure in case of a failed-open regulator event.

As described above, for an outlet pressure of 120 bar, the regulator outlet temperature is 260 K. To utilise the cooling from the first-stage expansion and to reduce transients, heat transfer from the parts between the regulator and the throat was minimised by placing these parts within a temperature-controlled unit, which was a commercial freezer (Tefcold GM 300), with holes for connections and access to manual actuators as shown on Fig. 3. By matching the initial cooling and temperature setpoint of the freezer, the temperature transition in the test unit could be significantly reduced.

The knowledge of the throat inlet temperature and pressure is essential for the definition of the boundary conditions of the test case with the underexpanded jet. The temperature was measured at the throat inlet by placing a 500- μm outer diameter type T mineral-insulated grounded thermocouple at the centre of the inlet of the test section. Due to the transient nature of the rig start-up, it is important to determine the thermocouple response time. Using the Churchill Bernstein heat transfer correlation, the heat transfer coefficient was estimated at 4800 W/m²/K. For a conductivity of 2 W/m/K (that of MgO the insulating material), the Biot number is estimated to be 0.6 which indicates that a transient spatially resolved heat conduction approach is necessary. Applying a method of separation of variables to a transient one-dimensional system in cylindrical coordinates resulted in an analytical solution based on Bessel functions (see Ref. Hahn and Necati Özisik 2012). The 50% and 90% response times of the thermocouple were estimated at 0.13 and 0.5 s, respectively. The accuracy of the thermocouple reading itself was assessed to be within 0.4 K from a two point calibration at -17°C (in the freezer) and 20°C (at room temperature) using a calibrated PT-100 probe as a reference.

The pressure was measured by a transducer (Omega PXM319-200G10V) with an accuracy of 2 bar and a response time of 1 ms. The sampling rates for the

thermocouple and pressure transducer measurements were 1.25 and 1000 Hz, respectively. Signals from the pressure transducer, the valve actuation voltage, as well as the camera recording were logged onto an oscilloscope for synchronisation. The thermocouple signals were separately read out by a thermocouple reader. The rising edge in the throat temperature trace caused by compression at the throat following the valve opening was used for synchronisation, yielding an uncertainty of 0.4 s for the timing of the temperature measurements, which is commensurate with the abovementioned thermocouple response time.

The evolution of the upstream conditions over time during the expansion is shown in Fig. 4. As shown, the set temperature of the freezer matched the temperature downstream of the first expansion (257 K). Both temperatures were lower than the temperature expected from the isenthalpic profile of Fig. 2 at 130 bar (approx. 265 K). This is due to the expansion work exerted by the fluid in the cylinder, which caused the cylinder internal temperature (not shown here) to decrease. At the throat inlet, the maximum pressure condition was reached after 2 s, and the temperature reached the near-steady condition after approximately 10 s, at 125 ± 1 bar and 259 ± 1 K, respectively. This experiment is therefore capable of providing steady temperature and pressure inlet conditions for over 50 s. From the inlet pressure and temperature, the minimum stagnation temperature downstream of the throat can be calculated with an isenthalpic expansion using the NIST database (REFPROP), which gives a value of 198 K. This system therefore allowed to exploit the full Joule–Thomson cooling from 300 to 1 bar.

To validate the boundary conditions, the theoretical mass flux was integrated in time and compared to the loss of pressure in the gas cylinder. The mass flux was estimated considering an isentropic expansion based on inlet pressure and temperature conditions using REFPROP and integrated over the duration of the experiment shown in Fig. 4. The pressure in the cylinder before the experiment was compared to the pressure in the cylinder 30 min. after the end of the experiment, and converted into mass difference using

REFPROP. The mass difference in the cylinder was 5.45 kg with a 3% uncertainty based on the gauge reading. The theoretical time-integrated mass-flux through the throat was 5.80 kg ($\pm 4.5\%$) with the main uncertainty contribution being the diameter of the throat, i.e. 1.535 ± 0.035 mm. The two results agree within the measurement uncertainty, validating the test rig operation.

3 Optical measurements

3.1 Schlieren measurements

Due to the very high pressure ratio expansion, a wide Mach disk was expected. A schematic of the compressible features of an underexpanded jet, reproduced from Crist et al. (1966), is shown in Fig. 7. Due to the small thickness of the normal shock (a few nm), and the high density ratio (> 5 for a PR > 100), the Mach disk corresponds to a strong density gradient which is easily visualised using Schlieren imaging.

For the Schlieren measurements, a test section with a traversing optical access was used. On the front side and on the back side, windows with a clear aperture of 27 mm (H) \times 52 mm (W) were mounted. A Z-shape Schlieren system with a 6° angle was formed using two 15-cm diameter $f = 1.2$ m parabolic mirrors as shown on Fig. 5. A “white” 800 mW LED (Thorlabs MCWHL5) pulsed by a driver (Thorlabs LEDD13) was used as a light source and focused on a rectangular aperture by a 50-mm $f/1.4$ Nikon objective, playing the role of light condenser. A CCD camera (La Vision Imager Intense) without camera objective and a $f = 250$ mm achromatic doublet were used to image the vertical mid-plane of the square test section with a field of view of 60 mm \times 40 mm. While the exposure time of the CCD camera was set to 10 μ s, the LED pulse duration was set to 500 μ s. This was to prevent charge accumulation during the long readout time of the CCD camera due to the relatively low extinction factor of the opaque coating of the interline storage pixels. If the LED was not pulsed, more

Fig. 4 Evolution of the temperature and pressure upstream of the throat during an expansion run with an initial cylinder pressure of 280 bar. The theoretical stagnation temperature post-expansion is also shown

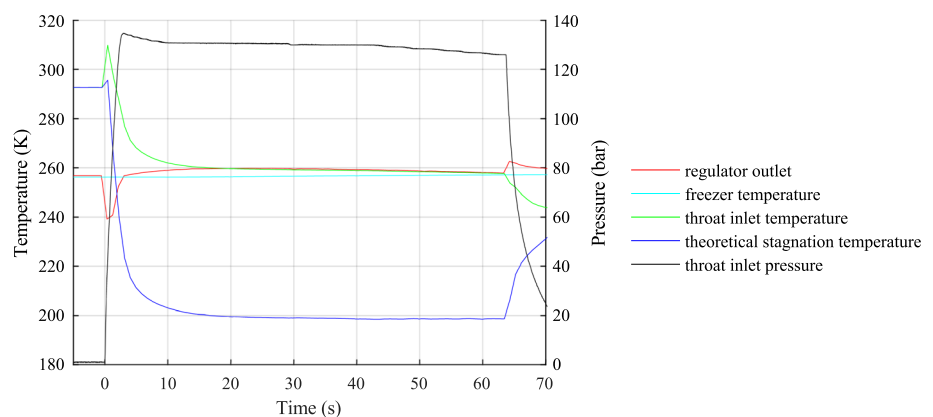
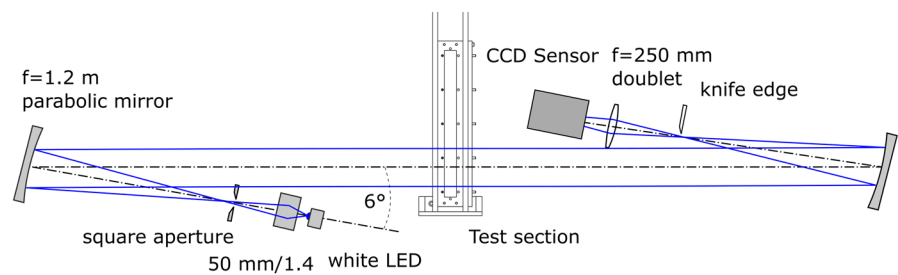


Fig. 5 Top view of the optical setup for the Schlieren measurements



than 80% of the signal would be accumulated during the readout time (~ 100 ms), with a severe loss in temporal resolution. To visualise the temporal evolution of the Mach disk instabilities, high speed Schlieren measurements were also performed by replacing the CCD camera with a CMOS camera (Photron SA-X2), allowing a frame rate of 540 kHz, for a region of interest of 40×120 pixels. A vertical knife edge was used, so that the intensity of the Schlieren image is proportional to the gradient of the index of refraction (hence density via the Gladstone–Dale relation) in the streamwise direction.

3.2 High speed particle image velocimetry

Velocity measurements were performed by particle image velocimetry. A test section with the same dimensions but with a different optical access was used, which is shown in Fig. 6. On the front side, a window with a clear aperture of $52 \text{ mm} \times 290 \text{ mm}$ allowed imaging the entire height of the test section from the bottom to the top wall. On the other side, a rectangular window with a clear aperture of $24 \text{ mm} \times 290 \text{ mm}$ permitted laser illumination. Both windows were machined with stepped edges so that they were flush with the metal sidewalls, maintaining symmetry within the channel and avoiding steps, which would induce local recirculation zones and perturbations to the flow near the walls. To minimise reflection from the top and bottom walls, in some of the measurements, instead of propagating the beam vertically, the beam was propagated horizontally from the exit of the test section using a periscope placed at the exit of the test section. The periscope was flushed with nitrogen to prevent particle deposition on the mirror. A comparison between measurements performed with either illumination path is presented in Sect. 4.3.2 to assess a possible influence of the presence of this periscope on the fluid flow. To obtain measurements at various positions along the 29-cm optical accessible part of the test section, the test section was translated while the illumination and detection systems were kept fixed. This resulted in a distance between the channel exit and the periscope which varied between 5 cm for the measurements near the throat to 27 cm for the downstream measurements.

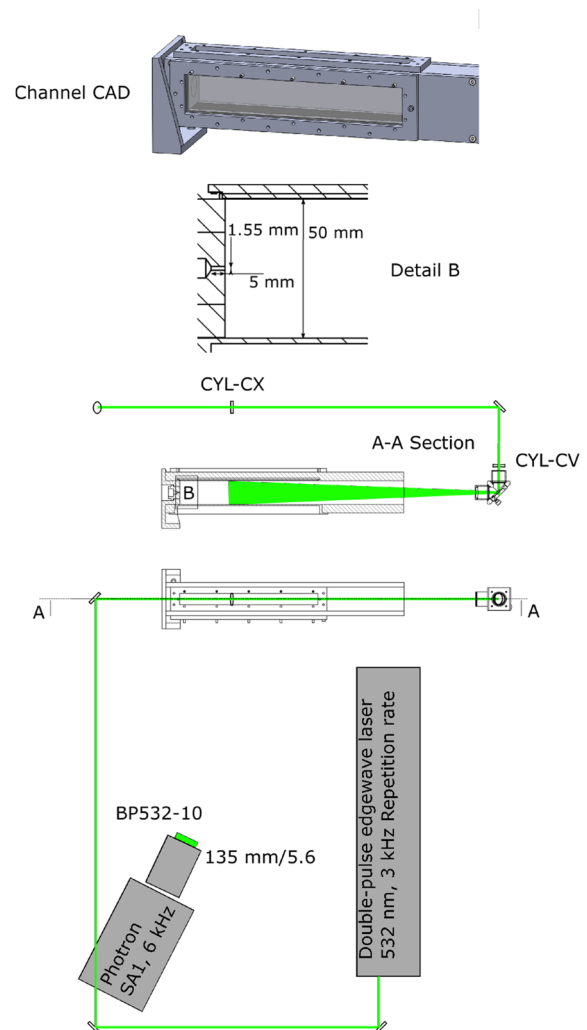


Fig. 6 Computer-aided design view of the test section (top) and schematic of the experimental setup for the PIV measurements (bottom)

Micron-size ZnO particles (Sigma-Aldrich 96476) were used as a seed material and introduced in the stream using the particle seeder described above. ZnO has a density of 5.6 g/cm^3 . Scanning Electron Microscope images of the particles can be found in Abram et al. (2015), which show that the particles form clusters with a primary size of 200 nm for a total span of 1–2 μm . The tracing ability

of such particles is expected to be far better than of $1\ \mu\text{m}$ spheres for which the velocity response time is approximately $20\ \mu\text{s}$ at room temperature. The volume-equivalent sphere diameter of the particles was measured by comparing particle number densities and mass concentrations in liquid suspensions after ultrasonic dispersion, resulting in about $600\ \text{nm}$. In the Stokes regime, we can estimate the response time to a stepwise increase in velocity using the equation of motion:

$$\frac{\pi d_V^3}{6} \rho_P \frac{dU_s}{dt} = -3\pi\mu d_H U_s, \quad (3)$$

where d_V is the volume-equivalent sphere diameter, d_H is the hydraulic diameter, and U_s is the slip velocity. The resulting relaxation time constant is

$$\tau = \frac{\rho_P d_V^3}{18\mu d_H}. \quad (4)$$

The sphere with an equivalent response time would therefore have an equivalent diameter of $\sqrt{\frac{d_V^3}{d_H}}$, which for a hydraulic diameter of $1.5\ \mu\text{m}$ results in a response time equivalent sphere diameter of $380\ \text{nm}$ and a response time of about $2\ \mu\text{s}$ at room temperature. To quantify the effect of particle lag in the comparison between simulations and experiments, spherical particles of two diameters ($380\ \text{nm}$ and $1\ \mu\text{m}$) were inserted in the simulations and the slip velocities are evaluated in Xiao et al. (2018). Further discussions of the errors induced by particle inertia are presented in Sect. 4.3.4.

Due to the high velocity and levels of recirculation encountered within the test section, a high rate of particle deposition on the walls and windows occurred, such that the measurement quality rapidly deteriorated over time. Therefore, the measurements were performed at $3\ \text{kHz}$ so that significant statistics (> 200 samples) could be rapidly obtained before deposition became an issue. For this, a double pulse Edgewave laser operated at $3\ \text{kHz}$ was used as a light source. The laser beam was formed into a $550\ \mu\text{m} \times 60\ \text{mm}$ light sheet at the test section using a combination of $f = 750\ \text{mm}$ and $f = -50\ \text{mm}$ cylindrical lenses as shown in Fig. 6. The laser fluence was set to $6\ \text{mJ}/\text{cm}^2$ per pulse. The delay between the two laser pulses was set to $2\ \mu\text{s}$ for all measurements. Images of the Mie scattered light from the particles were recorded by a Photron SA1.1 camera, operating at $6\ \text{kHz}$ with a region of interest of 1024×896 pixels. The camera was equipped with a Nikon $135\ \text{mm}/f/2.8$ lens operated at $f/5.6$ and a $532\text{-}10$ interference filter (notation is CWL-FWHM). The field of view was $60\ \text{mm}$ (H) \times $44\ \text{mm}$ (V) centred $5\ \text{mm}$ above the centerline of the test section. Using a Scheimpflug adapter, the camera imaged particles at a 76° angle with respect to the laser sheet plane. This is to make

space for a two-colour planar temperature imaging system at 90° , which would allow simultaneous temperature and velocity measurements as in Schreivogel et al. (2016) but which is not described in this article. Since it is shown in the following that the out-of-plane velocity component is small (5% of the axial component) the perspective error is neglected.

The particle image size was determined as $1/\sqrt{2}$ times the width of the autocorrelation peak of a single exposure recording (see Raffel et al. 2007), and was found to be 1.45 pixels on average. The seeding density is estimated to be between 1 and 4×10^{11} particles per m^3 , corresponding here to particle image densities of $0.15\text{--}0.6$ particles per pixel. The recorded images were mapped using a calibration target, and a multiple pass cross correlation algorithm with an intermediate window size of 4128×128 pixels was applied to determine the particle displacement field. Spurious vectors were removed by detecting vectors which have values that are more than two standard deviations away from neighbouring vectors and were not replaced. Unless stated otherwise, the final interrogation window was 32×32 pixels, and the overlap between windows is 50% for a final vector spacing of $800\ \mu\text{m}$. The effective spatial resolution according to Wieneke (2015) is 28 pixels or $1.4\ \text{mm}$.

4 Results

4.1 Compressible features in the near field

An example of a Schlieren image obtained for a cutoff of 0% at an absolute inlet pressure of $112\ \text{bar}$ is shown in Fig. 8. The bright zones correspond to high index of refraction gradients in the streamwise direction, such as for the compression waves, and for the Mach disk. The distance from the throat to the Mach disk is estimated from the location of the local maximum gradient (or minimum Schlieren intensity). The location of the Mach disk was measured for different values of the pressure ratio (PR) between 60 and 122 and compared to the location predicted by the empirical relation derived by Crist et al. (1966)

$$H_m \approx 0.67 \times D \times \sqrt{\text{PR}}, \quad (5)$$

where D is the throat diameter.

The results, which are plotted in Fig. 9, show a good agreement, although the Schlieren results are consistently slightly higher than the correlation for values of the PR above 80 , with a difference of 3.6% at a PR of 120 . Fluctuations in the Mach disk location were observed. For a PR of 120 , based on 1000 measurements, the Mach disk distance varied from 11.5 to $12.5\ \text{mm}$, with a standard deviation of $0.15\ \text{mm}$. These measurements validate the jet boundary

conditions. Note that the Schlieren measurements represent the axial density gradient which are line-averaged over the transverse direction.

When performing the PIV measurements, recording the scattered light under 532-nm illumination, very bright regions were noticed near the throat. Example images are shown in Fig. 10. A very homogeneously distributed intensity was measured in the centre of the jet up to a streamwise distance of 12 mm. Note that the upstream (or left) edge of this zone corresponds to the edge of the vertically propagating laser sheet for that measurement. On either side of the jet centre, sharp bright shedding features were also observed which may correspond to the outer supersonic region (see Fig. 7). The Mach disk corresponds to a sharp increase in the gas density (by over a factor 5 across the shock at $PR = 120$ based on normal shock relations). Therefore, the scattering signal from particles should strongly increase across the Mach disk in the downstream direction. Indeed, in Chauveau et al., where PIV measurement with TiO_2 particles were performed in a high stagnation temperature (post-combustion) underexpanded jet, a strong increase in particle signal was observed across the Mach disk (Chauveau et al. 2006). However, the bright regions of Fig. 10 correspond to supersonic regions, where low particle densities are expected and it is thus suspected that the scattering signal originates from argon nucleation. In contrast to the current study, Chauveau and co-workers did not observe nucleation simply because their stagnation temperature was much higher so that subcritical temperatures were not encountered. Baab et al. analysed from a thermodynamic standpoint expansions of n-hexane jets from supercritical to subcritical pressure under various stagnation temperature conditions and used elastic light scattering to reveal zones of multiphase flows (Baab et al. 2018).

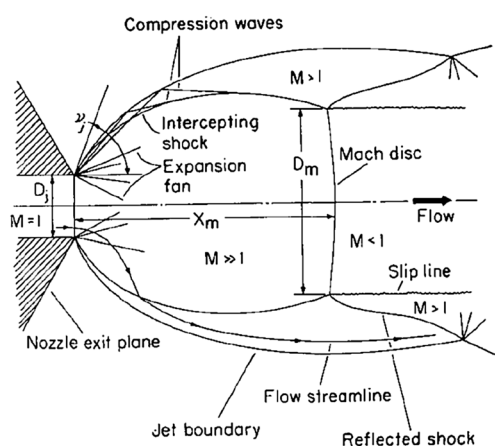


Fig. 7 Schematic of a free underexpanded jet, reproduced from Crist et al. (1966)

A temperature–entropy diagram for argon is drawn on Fig. 11. Assuming an isentropic expansion from the throat inlet to the Mach disk, this initial process is represented by the vertical line starting from supercritical conditions at 120 bar and 273 K. This isentropic line crosses the saturated vapour line at 15.1 bar. Since the Mach disk is a strong compression, and the downstream pressure is atmospheric, it is clear that the expansion crosses the two-phase region of the diagram. However, this temperature–entropy diagram is only valid at equilibrium and does not account for the kinetics of the nucleation process and the irreversibilities associated with the droplet growth process. Nucleation in low temperature supersonic flows was studied by several groups (Matthew and Steinwandel 1983; Koppenwallner and Dankert 1987; Sinha et al. 2010). Conditions at which the onset of nucleation was observed in Sinha et al. (2010) are plotted in a pressure–temperature diagram in Fig. 12. Nucleation

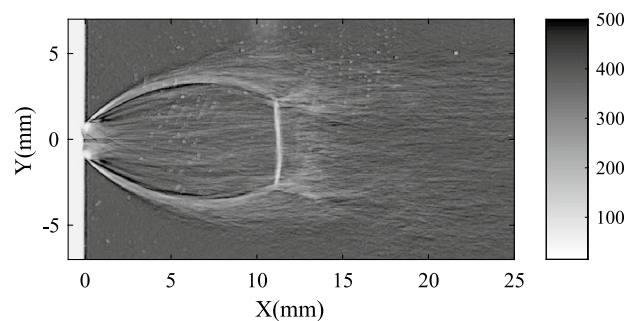


Fig. 8 Schlieren image obtained for an upstream pressure of 112 bar

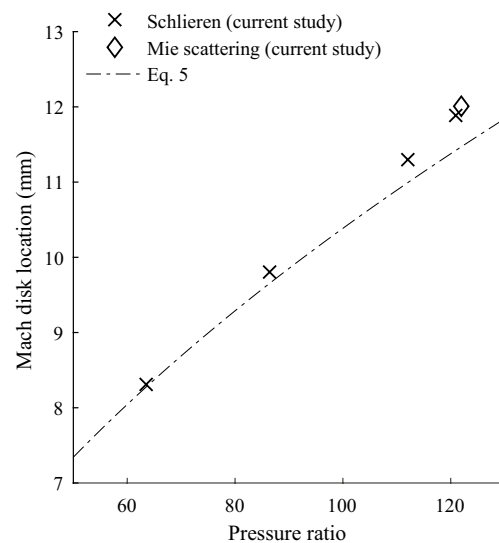


Fig. 9 Mach disk location measured at various pressure ratios and comparison with Eq. (5)

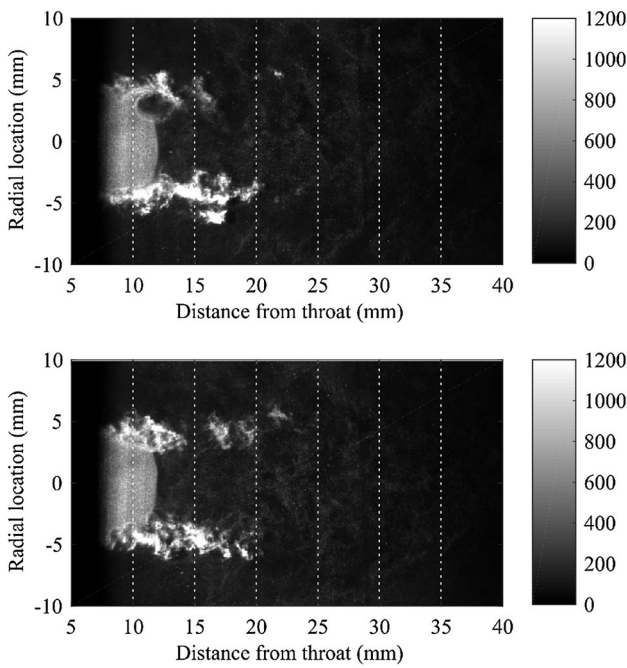


Fig. 10 Two separate single-shot images of the Mie scattering intensity in the near-throat region (left). The upstream pressure was 125 bar and the laser was propagated from the top. The upstream edge of the bright zone at 7.5 mm is induced by the edge of the laser sheet

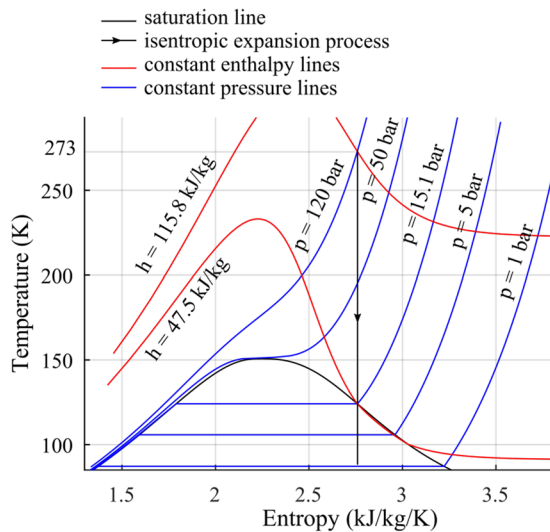


Fig. 11 Entropy–temperature diagram for argon. A line corresponding to an isentropic expansion starting at the throat inlet condition 273 K and 120 bar is drawn

requires supersaturation so the onset of nucleation at a given pressure is observed at a lower temperature than the saturation temperature. To compare these conditions to the fluid flow of the current study, the results of single-phase real gas CFD simulations presented in Xiao et al. (2018) are shown in Fig. 12 for locations along the jet centerline from the left

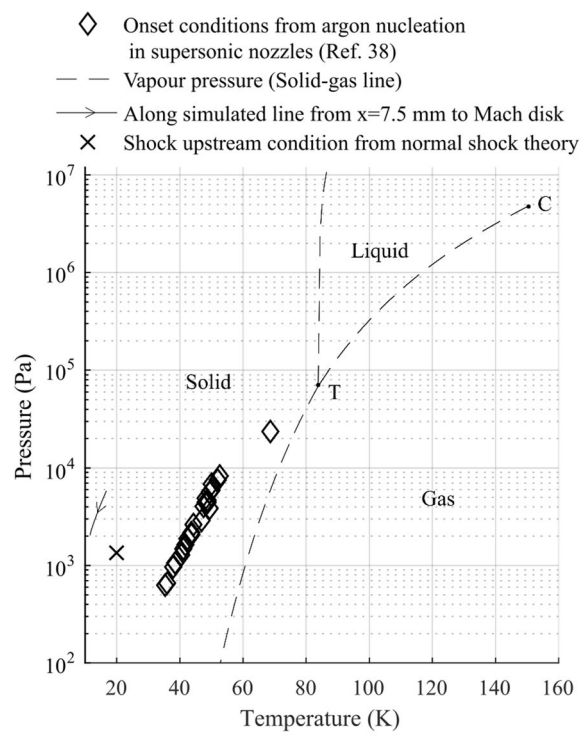


Fig. 12 Pressure–temperature diagram for argon. The conditions for the onset of nucleation observed in Sinha et al. (2010) in supersonic nozzle experiments are also plotted together with results of 3D single-phase real gas CFD simulations (Xiao et al. 2018) and the shock upstream conditions derived from the theory of normal shock in perfect gases

edge of the laser sheet ($x = 7.5$ mm) to the Mach disk location. In comparison, normal shock relationships for perfect gases for a stagnation pressure ratio of 120 predict a Mach number of ~ 8 upstream of the shock with a minimum temperature of 20 K and a minimum pressure of 1300 Pa. As shown in Fig. 12, both the conditions predicted by the simulations over the illuminated area upstream of the shock and the conditions predicted by the theory of normal shock for perfect gas are far more favourable to nucleation than the onset conditions observed by Sinha et al. (2010), therefore the presence of a condensed phase (droplets or crystals) is a likely explanation for the bright regions observed in Fig. 10.

Assuming that the scattered light upstream of the Mach disk in Fig. 10 is caused by condensation, the location of the Mach disk could be extracted from this spatially resolved (and not line-of-sight averaged) measurements by determining the axial position at the centerline where the intensity reaches the arithmetic mean of the intensities in the bright and dark regions. The mean disk distance was measured as 12.0 mm with a standard deviation of 0.3 mm. Larger fluctuations are observed in the Mach disk location derived from the scattering images than from the Schlieren measurements. This is expected since Schlieren measures

the gradient averaged over the line of sight, therefore averaging over the locally fluctuating mach disk surface. The minimum and maximum distances measured were 11.1 and 12.7 mm, respectively. As shown in Fig. 9, this value is in very good agreement with that derived from the Schlieren measurements.

4.2 Velocity measurements

4.2.1 Global flow structure

Measurements were performed in three regions: (1) the near throat region ($x = 10\text{--}60$ mm, where x designates the streamwise distance from the throat exit) where high velocities and little thermal mixing in the core are expected and which is referred to as the near-field, (2) a middle region ($x = 110\text{--}160$ mm), which is referred as the “impingement region”, where the jet boundaries are expected to reach the wall based on free jet theory so that the maximum heat transfer rate is expected and (3) a downstream region ($x = 230\text{--}280$ mm), which is referred to as the “fully-developed” region where the velocity profile is expected to resemble that of a fully developed turbulent channel flow. The measurements were performed over a 1-s window, approximately 5 s after the valve opening (see Fig. 4). At each location, average fields were established from the measurements. Considering the measured fluid velocity vector being

$$\vec{v}(x_i, y_j, t_k) = v_x \vec{i} + v_y \vec{j}, \quad (6)$$

where x_i and y_j are the discrete measurement locations and t_k denotes the discrete measurement instants. The mean axial velocity is calculated as:

$$\bar{v}_x(x_i, y_j) = \frac{1}{N} \sum_{k=1}^N v_x(x_i, y_j, t_k), \quad (7)$$

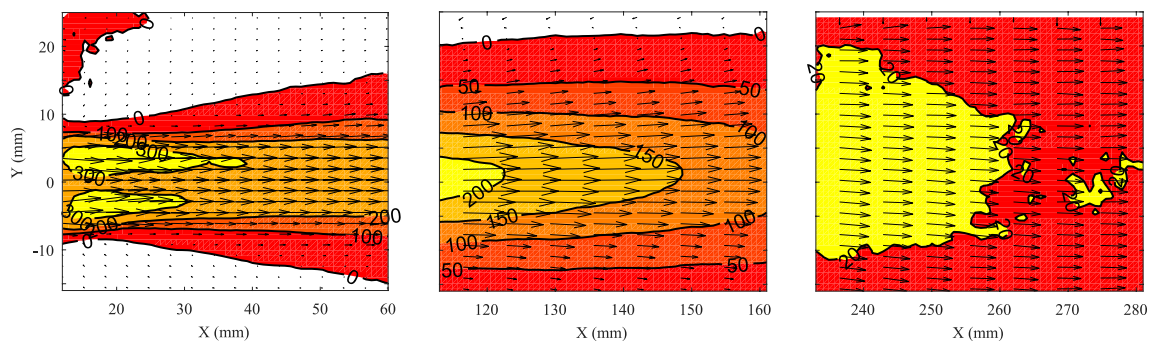


Fig. 13 Average velocity fields in the three measurement regions. The contours represent the absolute value of the streamwise velocity component, so that the 0 contour encloses a region of negative streamwise velocity, which here is indicated in white. Note that different scales are used for the three velocity vectors in the three regions, and that

where N is the number of samples. Average flow fields for the three regions are shown in Fig. 13. Note that the field of view is not centred on the centerline. Due to the wide range of velocities, the three regions apply different vector length scales, and the contours and colours serve to indicate the scale of the streamwise velocity component. The flow evolves from a jet with a very high velocity (> 200 m/s), surrounded by a large recirculation, to a homogeneous low-velocity channel flow (20 m/s). The intermediate region is the focus of this study as this is where initial wall temperature measurements using thermocouples, not shown here, have indicated the strongest wall cooling. This region shows a fast and continuous decay of the centerline velocity, i.e. from 200 to 150 m/s within 2.5 cm. From this global picture of the flow, we can identify the extent of the recirculation zone, and determine the spreading angle based on the jet half-width, which is the radial location where the jet velocity has decayed to one half of its centerline value. The recirculation zone extends over a distance of at least 160 mm behind the exit of the orifice. Based on the location $x = 125$ mm, using the 200 m/s and 100 m/s contour of Fig. 13, the jet half angle is determined to be approximately 4.8° . These measurements can be used for an estimation of Reynolds number by comparing the flow downstream of the Mach disk with a turbulent jet exiting from a nozzle. At a location of $x = 30$ mm, the flow may be approximated by a free jet, with a velocity of at least 200 m/s over a diameter of 16 mm, which, for argon at 220 K and 1 bar, results in an estimated Reynolds number of over 400,000.

4.2.2 Turbulence characteristics in the impingement region (110–160 mm from throat exit)

Examples of consecutive single-shot measurements in the impingement section, which is the main focus in this study, are shown in Fig. 14. Highly contorted pockets of high

only every eighth vector is plotted in the streamwise direction (x) while every second vector is plotted in the transverse direction (y) for clearer visualisation. Note that the field of view is not centred at the centerline

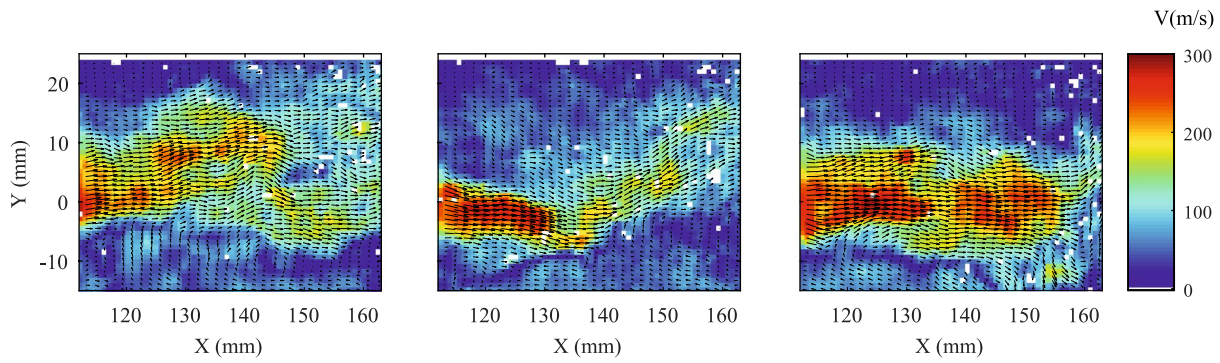


Fig. 14 Three consecutive (but uncorrelated) single shot velocity fields in the impingement region for a sampling rate of 3 kHz. The colour bar corresponds to the magnitude of the velocity vector. Only

every second vector is displayed in the axial direction. The locations of measurements which were rejected by the median filter are represented as white pixels

velocity fluid in the range 220–350 m/s are observed in locations which strongly vary from one measurement instant to another. The extent of the pockets is approximately 10 mm on average, which can be used as a first approximation of the integral length scale. It is likely that out-of-plane motion plays a large role in the observed intermittency, where the alignment between the jet core axis and the measurement plane produces the highest measured velocity magnitude. Note that despite the relatively high sampling rate of 3 kHz, the displacement of a flow element would be about 50 mm between two consecutive measurements at an average velocity of 150 m/s. Considering an integral length scale on the order of the height of the test section, two measurements are thus only weakly correlated.

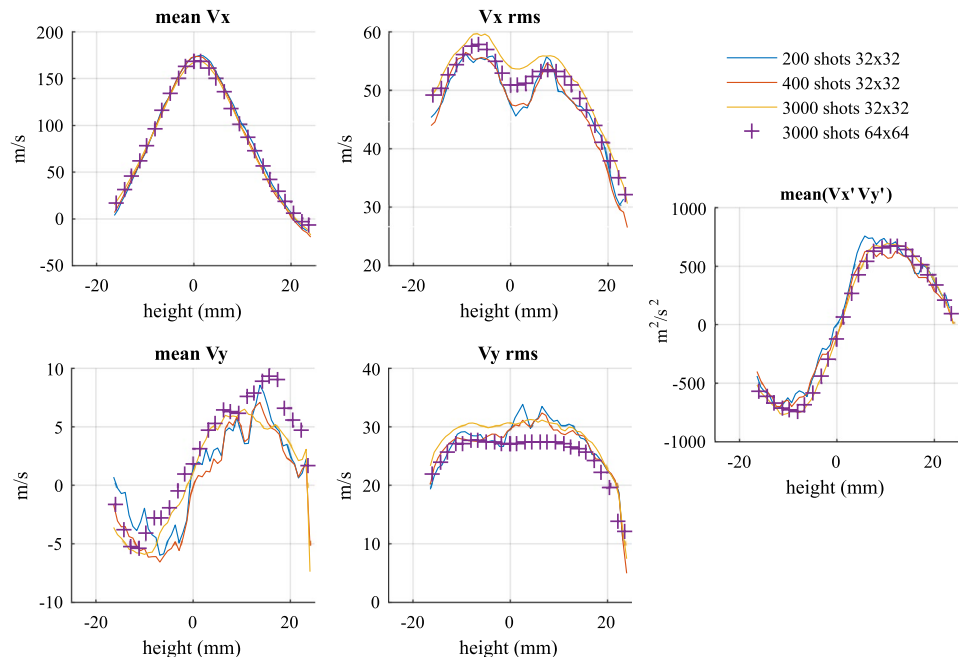
To provide further quantification of the turbulent characteristics of the flow, the root mean square of the axial velocity component and the mean fluctuation term $\overline{v'_x v'_y}$ (where v'_x and v'_y are the fluctuating components of the axial and transverse velocities, respectively, were also calculated. The root mean square velocity fluctuation field is derived as:

$$v'_{x,rms}(x_i, y_j) = \sqrt{\frac{1}{N} \sum_{k=1}^N [v_x(x_i, y_j, t_k) - \overline{v_x}(x_i, y_j)]^2}, \quad (8)$$

and the Reynolds stresses as:

$$\overline{v'_x v'_y}(x_i, y_j) = \frac{1}{N} \sum_{k=1}^N [(v_x(x_i, y_j, t_k) - \overline{v_x}) \times (v_y(x_i, y_j, t_k) - \overline{v_y})]. \quad (9)$$

Fig. 15 Transverse profiles of the first and second order velocity statistics at location $x = 140$ mm; the measurements are sampled at 3 kHz



Sampled transverse profiles are shown in Fig. 15 for different interrogation areas (32×32 and 64×64) or number of samples. Note that the channel height coordinate starts at a wall at -25 mm and ends at a wall at $+25$ mm. In all sets, the axial velocity has a peak centred at the centerline. There is a recirculation zone at the top part and probably also at the bottom part, although the latter cannot be confirmed due to the absence of measurements below -15 mm. The axial velocity fluctuations show two maxima at about 55 m/s on either side of the centerline, at a distance of 6 mm corresponding to turbulence intensities above 30% . A slightly higher peak fluctuation is observed in the bottom half than in the upper half. Profiles of the mean and fluctuating cross stream velocity, v_y , are also plotted on Fig. 15. The mean cross stream velocity shows an asymmetry with higher values on the upper part of the test section. The cross-stream velocity fluctuations show a flat profile from -10 mm to $+17$ mm at about 30 m/s, which is about half of the axial velocity fluctuation in that region. Finally, the magnitude of the Reynolds stress has maxima in the upper and lower shear regions, with an outward momentum flux of approximately $700 \text{ m}^2/\text{s}^2$ in the top half and $750 \text{ m}^2/\text{s}^2$ in the bottom half. This is in line with the gradient diffusion hypothesis since a larger gradient in the mean axial velocity was observed in the bottom half. The Reynolds stress is zero at the centerline,

as expected from symmetry and tends to zero towards the upper wall.

In addition to the first and second moments as shown here, the shape of the probability density function of the velocity can provide further insight in the turbulence structures, when a comparison is made with the results obtained from Large Eddy Simulations (LES), which is the chosen method to simulate this flow. For this purpose, histograms of the measured axial velocity were compiled at three specific locations near the top wall, and three locations on the centerline using an ensemble of 3000 single shot velocity fields; the results are shown in Fig. 16. The ability to provide such large sample numbers within a reasonable time span is afforded by the high sampling rate of the imaging system (3 kHz). The mean values of those distributions are represented by the red bars. At the three locations near the wall, the velocity distribution is normal-like with the mean value decreasing from -16 to -5 m/s, and the standard deviation from 33 to 22 m/s from $x = 115$ mm to $x = 160$ mm as the recirculation zone ends. At the centerline, however, the velocity distribution shows a significant asymmetry at $x = 115$ mm with a longer wing on the low velocity side, which then evolves to a more normal-like distribution further downstream. It is interesting to note that at $x = 160$ mm on the centerline, there are even instances, accounting

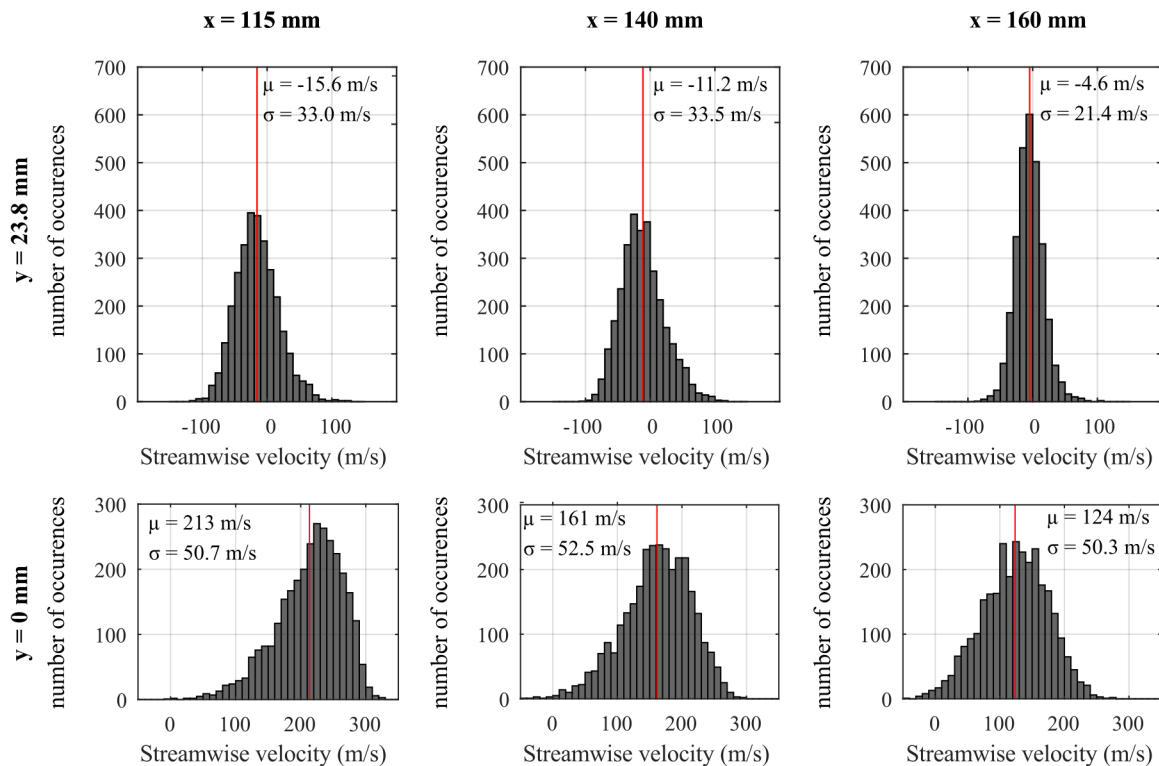


Fig. 16 Histograms of the streamwise velocity at six locations, three near the top wall and three on the centerline, extracted from an ensemble of 3000 velocity fields recorded at 3 kHz. Each bin corre-

sponds to a range of 10 m/s. The red vertical lines designate the mean of the distributions. The value of the mean and standard deviations are also indicated

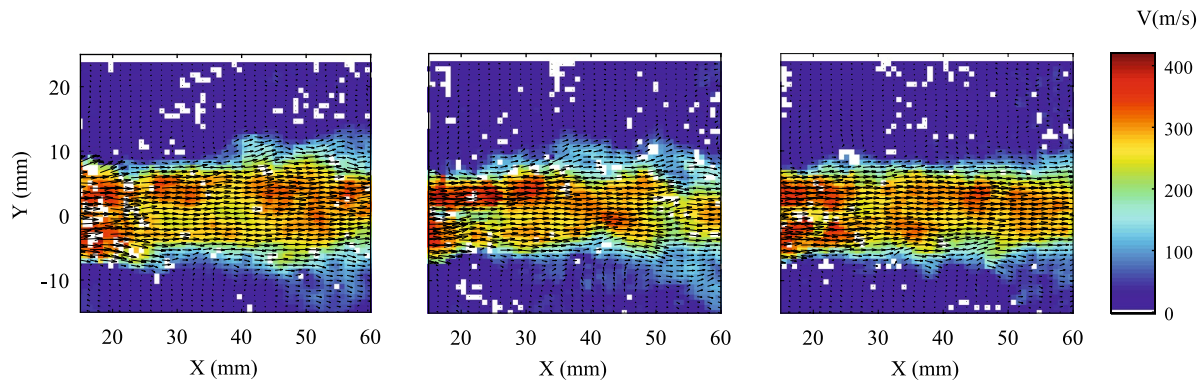


Fig. 17 Consecutive (but uncorrelated) single shot velocity fields in the near-throat region for a sampling rate of 3 kHz. The color bar corresponds to the magnitude of the velocity vector. Only every second

vector is displayed in the axial direction. The locations of measurements which were rejected by the median filter are represented as white pixels

for about 1%, of back-flow (negative velocity), which is an indication of the significant degree of intermittency.

4.2.3 Turbulence characteristics in the near-throat region (10–60 mm from throat exit)

Examples of consecutive (but uncorrelated) single shot measurements in the near throat region are shown in Fig. 17. Supersonic peak velocities of over 420 m/s are measured. Here, unlike in the impingement region, the extent of the intermittent regions is far smaller and the high velocity core is confined to a 10-mm width at the channel center.

The profiles of the first and second moments are shown in Fig. 18. As shown in the profile of the first moment, a high velocity jet core is present, and there is a large recirculation zone starting 10 mm above the centerline. From the asymmetry in the shape of the wings of the velocity profile, the jet core seems to be slightly pointing downward. The root mean square velocity, or second moment shows a peak in the jet shear regions, 4–8 mm from the centerline on either

side, with a value of about 80 m/s. A slightly higher value is observed in the upper part than in the lower part. The turbulent flux also shows a peak in the shear region, where the highest momentum transfer takes place, which slows down the jet. The outward flux is about 30% higher in the upper part than in the lower part, which seems consistent with the higher mean velocity gradient in the upper part.

4.3 Uncertainty analysis

To allow for a meaningful comparison between the measurements and the results of numerical simulations, various aspects which may influence the measurements are assessed, such as the sample size, the size of the interrogation area, the intrusive character of the periscope and the experiment repeatability. An analysis of velocity measurement uncertainty based on correlation statistics is also provided, as well as an analysis of the errors resulting from the particle inertia.

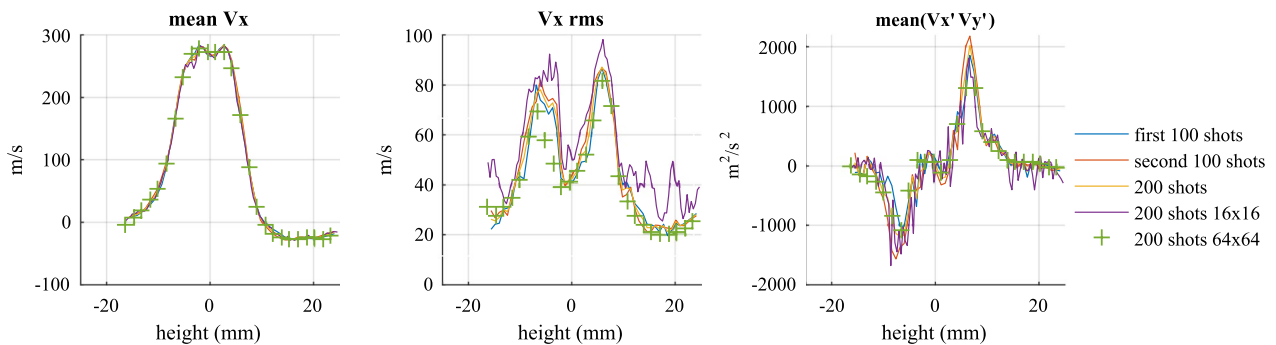


Fig. 18 Transverse profiles of the mean axial velocity, root mean square axial velocity fluctuations, and average fluctuation products at the location $x = 25$ mm, measurements are sampled at 200 Hz. Note

that there was no periscope at the channel exit and the illumination was vertical for these datasets

4.3.1 Data convergence

For a single expansion run, where 3000 images were recorded, statistics were compiled over different sample lengths to assess the convergence of the velocity statistics. The transverse profiles of mean axial and transverse velocity, their root mean square fluctuations, and turbulent flux terms obtained at $x = 140$ mm for those different samples were shown in Fig. 15. As mentioned above, two consecutive measurements are mostly uncorrelated. Very little difference in the first moments of the axial component of the velocity is observed between the different sample sizes, but there are larger relative differences in the mean cross-stream velocity. The relative velocity uncertainty is higher for the cross-stream velocity than for the axial velocity, due to the lower range of velocities and therefore longer sample sizes have more effect in reducing the uncertainty in the estimation of the mean value. The results for the second moment (rms velocity) of the axial component have slightly larger differences, within 10%, but all display a higher peak in the bottom part. The comparison of the turbulent flux $\overline{v'_x v'_y}$ shows very little difference in the amplitude between all sets, in which longer sample sizes provide a less noisy profile. The size of the interrogation area has very little influence for identical sample sizes other than the 5% decrease in the rms velocity observed in the centre part with the larger interrogation area, which is presumably due a combination of two effects: a reduced correlation-based uncertainty and a low-pass filtering of fine scale turbulent fluctuations due to the size of the interrogation area. In view of the small differences, these results confirm that 200 shots and an interrogation area of 32×32 would already allow a sufficiently low statistical uncertainty in the first and second moment statistics for the axial velocity. For the cross-stream velocity, larger sample sizes are preferable. For the sake of brevity, in the following, only the moments of the axial velocity and the coupled fluctuation terms are presented.

In the near-throat region, different sample sizes were also compared, using a total of only 200 images. For this

particular experiment, the recording was performed at 3 kHz, but only every 15th image was saved, so that the sampling rate of the data displayed is 200 Hz. Profiles extracted at $x = 25$ mm were shown in Fig. 18. For these data, there was no periscope and the laser beam was propagated vertically through the top window shown in Fig. 6. Due to the high velocity of 300 m/s, it is also evident that two such consecutive samples are uncorrelated. The mean velocity and rms data show very little difference between the three sampling windows, with the main noticeable feature being a higher peak turbulent flux in the second window. The size of the interrogation area does play a small role in resolving the local minimum in the axial velocity at the centerline, as the local minimum is absent with the 64×64 interrogation area and present with 32×32 and 16×16 interrogation areas. In the root mean square velocity profile, the magnitude of the fluctuations seems unchanged in the 32×32 interrogation area when compared to the 64×64 interrogation area, but the 16×16 interrogation area shows higher values due to a higher correlation-based uncertainty for this window size, which is particularly evident in the low velocity area found 10 mm above the centerline. In the turbulent flux profile, the larger interrogation area also misses the local inverted maxima in the inner shear region at $x = -3$ and $x = +3$ mm, but away from this region, the magnitude of the flux seems to be relatively unaffected by the size of the interrogation area. As expected, the 16×16 area shows a noisier profile. It can be concluded that the 32×32 interrogation area with a sample number of 200 images gives a sufficient degree of convergence and these results can be used for the validation of numerical simulations.

4.3.2 Effect of the periscope, illumination and repeatability

To assess the influence of the presence of the periscope on the flow field, measurements were performed with and without the presence of the periscope at the exit of the test section, both with a vertical illumination in the impingement region (at $x = 140$ mm). The results are shown in Fig. 19,

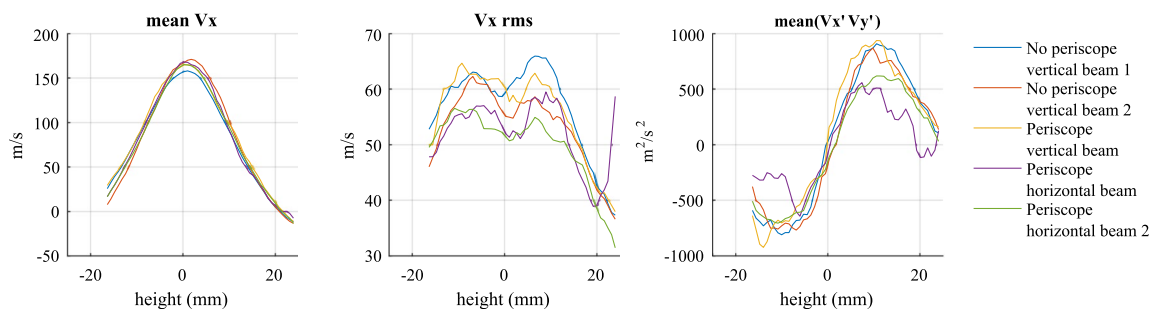


Fig. 19 Transverse profiles of the mean axial velocity, root mean square axial velocity fluctuations, and average fluctuation products at the location $x = 140$ mm for five separate experiments, with and without periscope, and with horizontal or vertical beam propagation

which include two repeated sets with vertical illumination and without periscope. In the average velocity profiles, the largest differences, which are still within 10 m/s, are noticed between the two repeated sets without the periscope. The same is true for the rms profile, while very little differences are observed in the Reynolds stresses between the three sets. The presence of the periscope has therefore a negligible effect on the flow field.

With the periscope at the exit of the test section, measurements were also performed to compare vertical and horizontal illuminations. Here the measurements with the periscope and the horizontal illumination were repeated. The mean axial velocity is unaffected while the root mean square velocity for the horizontal illumination is slightly lower by about 8% in the bottom shear layer in comparison with the vertical illumination for both repeated sets. One of the sets with the horizontal illumination shows a consistently lower turbulent flux by about 30% than the other sets but this is not confirmed by the repeated set under the same conditions. Based on those sets, the uncertainty in the mean velocity is estimated at 10 m/s, that in the root mean square velocity at 10%. A conservative estimate of the uncertainty in the turbulent flux is around 30%.

For the measurements in the near-throat region, the test section was translated. For the horizontal illumination, this means that the distance between the exit of the test section and the periscope has become smaller than in the previous case, namely 50 mm instead of 150 mm, which increases the likelihood that the periscope will cause a disturbance. Span-wise profiles obtained without periscope and vertical illumination are compared to profiles obtained with the periscope and horizontal illumination in Fig. 20. The mean axial velocity profile measured with the periscope shows a larger peak value (+ 19%) and a relatively lower centerline value than measured without the periscope. The recirculation region at the top also seems to be smaller with the periscope. In the root mean square velocity profile, larger peak fluctuations (+ 14%) are found without the periscope. The turbulent fluxes show the same profile shape, but the peak in the bottom

outer shear layer is 34% lower without the periscope while the peak in the upper outer shear layer is reduced by 50%. The local maxima in the turbulent flux in the inner shear layer are larger with the periscope, which is consistent with the deeper central valley obtained in the mean velocity profile with the periscope. The large deviations found between the different profiles show that measurements in the near-throat region can only be used for a qualitative comparison with simulations.

4.3.3 Random uncertainty of velocity measurements

It is important to evaluate the contribution of the random measurement errors to the observed velocity fluctuations. Several parameters, such as the level of the camera noise relative to the peak particle intensities, the seeding density, the particle image size and the size of the interrogation area, influence the random uncertainty in the measurements of the velocity field. To quantify the uncertainty, the DaVis 8 software uses an algorithm based on dewarping the second image of the cross correlation into the first one and shifting the peak of the correlation function (Wieneke 2015). This method of uncertainty quantification was compared with other methods and found to be the most adequate, with error estimation within 85% accurate over the conditions of this experiment (0.15–0.6 particles per pixels, particle image size above 1 pixel) (Sciacchitano et al. 2015). Profiles of random uncertainty in the axial and cross-stream velocity are shown in Fig. 21. For an assessment of the quality of the PIV measurements, it may be useful to note that 10 m/s corresponds to a 0.4 pixel displacement. At $x = 140$ mm, the profile of the axial velocity uncertainty is flat at about 7 m/s, which is about 13% of the root mean square velocity fluctuations measured close to the centerline, increasing to 50% close to the wall. The uncertainty of the velocity in the near-throat profile at $x = 25$ mm is higher than at $x = 140$ mm which is presumably due to the higher velocity gradient. The larger shear can cause a loss of correlation for the undistorted interrogation area used here. Nevertheless, in comparison

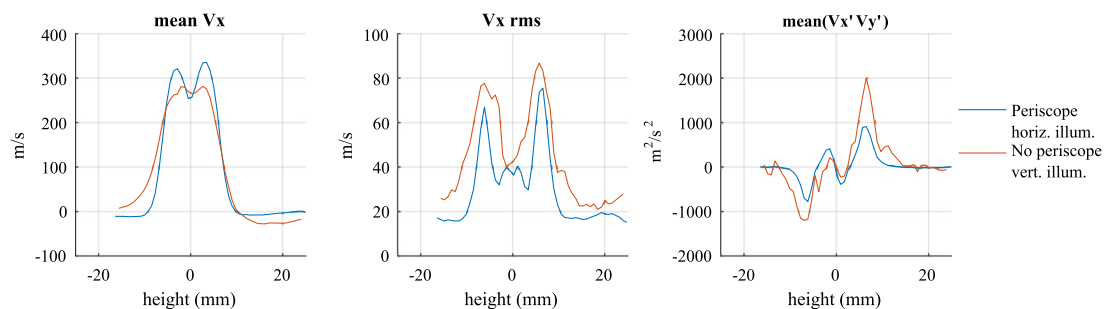


Fig. 20 Transverse profiles of the mean axial velocity, root mean square axial velocity fluctuations, and average fluctuation products at the location $x = 25$ mm with periscope and horizontal illumination and without periscope and vertical illumination

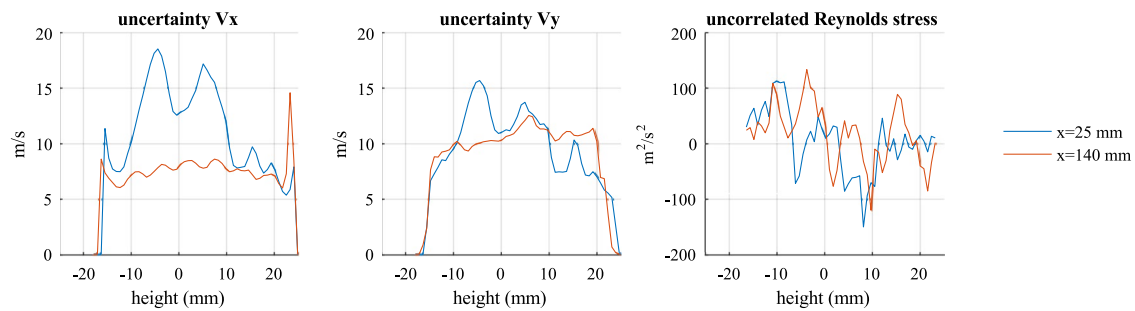


Fig. 21 Random uncertainty in axial and streamwise velocity, and average fluctuation products for uncorrelated axial and transverse velocities

with the root mean square velocity profiles of Fig. 18, the random uncertainty is below 25% of the RMS velocity in the centre part of the jet ($y = -10$ mm to $y = +10$ mm). This random uncertainty increases to about 50% in the low velocity region around the jet, which is because the lower velocity produces a lower particle displacement. The random uncertainty in the cross-stream velocity is relatively similar at the two locations, and represents about 37% of the measured root mean square cross-stream velocity fluctuations.

Through considering that the total uncertainty is the sum of two independent effects, we can assess that the contribution of the random uncertainty to the total root mean square fluctuations is for the axial velocity about 3% at the location of the peaks in the near-throat region and about 1% in the impingement region. The contribution increases to about 13% in the low velocity zones for both regions.

To assess the statistical significance of the correlation in the mean fluctuation product $\overline{v'_x v'_y}$, a mean product of uncorrelated data was calculated by imposing a separation of ten frames between the axial and transverse fluctuating components of the velocity. The results are also shown in Fig. 21. As expected, the mean product of the two uncorrelated variables fluctuates randomly, within $120 \text{ m}^2/\text{s}^2$, corresponding to about 15% of the peak values of the measured fluctuation product for the correlated variables.

4.3.4 Tracer particle inertia

The particle inertia can cause a deviation between the measured particle velocity and the actual flow velocity. Three situations can be considered: (1) a particle going across a strong velocity discontinuity such as a shock, (2) a particle entrained in a flow field described by a sinusoidal velocity fluctuation at a fixed frequency, and (3) a particle in a continuously accelerating fluid. The two first scenarios are well described in the article of Melling considering the particles in a Stokes drag law regime (Melling 1997). Here we consider 380 nm and 1 μm as the lower and upper bounds, respectively, for the flow-tracing-equivalent sphere diameter (see Sect. 3.2). For a particle going across a normal shock for argon with a stagnation

pressure ratio of 120, as being representative of the Mach disk, the upstream velocity is in the order of 600 m/s and the downstream velocity about 50 m/s. A 380-nm and a 1- μm spherical particle would reach 95% of the downstream velocity at a distance of 1.1 and 12 mm from the shock, respectively. For a particle in a fluid with turbulent velocity fluctuations at 6 kHz, the ratio between the particle rms velocity and the flow rms velocity is 95% and 76%, for the 380 nm and 1 μm spherical particle, respectively. Here, the measured fluctuations are an underestimate of the real flow fluctuations. Finally, for a particle following a flow with a streamline of constant acceleration, the particle slip velocity is constant and equal to $U_s = \tau \times a$, where a is the fluid acceleration and τ the relaxation time constant of Eq. 4. Approximating the flow deceleration in the impingement region $x = 110 - 160$ mm by a constant value of $620,000 \text{ m/s}^2$, the resulting slip velocity is 2 and 12 m/s for 380 nm and 1 μm spherical particles, respectively. In these calculations, the viscosity of argon was evaluated at 200 K and atmospheric pressure. In conclusion, in the vicinity of the near-shock region, large deviations between the velocity measured by the particles and the actual flow velocity are expected. In the impingement region, very little error in the average velocity is expected but a possible underestimation of the velocity fluctuations should be considered in the validation of numerical simulations.

4.3.5 Uncertainty summary

A summary of the uncertainty quantification of this section is given in Table 1. First, the contributions of the random fluctuation to the magnitude of the peaks of the second moment and flux are calculated based on the contribution of two random variables. The uncertainty in the measured statistics established from comparing values measured under different conditions is also shown in the table, as well as the conclusions of the considerations on the tracer particle inertia.

Table 1 Summary of the uncertainty contribution to the first moment, the second moment and the Reynolds stresses

| Region | Error type | $\overline{v_x}$ | $v'_{x,rms}$ | $\overline{v_y}$ | $v'_{y,rms}$ | $\overline{v'_x v'_y}$ |
|-------------|---|------------------|---------------|------------------|---------------|-------------------------------------|
| Near-throat | Contribution from random PIV uncertainty | – | 3% | – | 8% | 1% |
| | Uncertainty (repeatability and intrusiveness) | 50 m/s | 12 m/s | 7 m/s | 14 m/s | 1000 m ² /s ² |
| Impingement | Contribution from random PIV uncertainty | – | 1% | – | 6% | 1% |
| | Uncertainty (repeatability and intrusiveness) | 10 m/s | 5 m/s | 5 m/s | 7 m/s | 380 m ² /s ² |
| | Tracing uncertainty | 2–12 m/s | 5–24% @ 6 kHz | – | 5–24% @ 6 kHz | 5–24% @ 6 kHz |

For the second moment and Reynolds stresses, the errors are quantified on the peak values

5 Conclusions

A thorough understanding of fluid-to-wall heat transfer phenomena in confined highly underexpanded real gas jets is important for the safety of many processes in the oil and gas industry. It is a considerable challenge to accurately model this in a computational fluid dynamics (CFD) simulation. For the purpose of model development and validation, a test case was defined, which consists of a steady-state high-pressure ratio (PR \sim 120) expansion of argon in a square channel. The rig layout and control strategy were discussed. Thermocouple and pressure measurements confirmed the steadiness and repeatability of 60-s long measurement runs, offering well-defined boundary conditions for the numerical simulations. A particle seeder was also designed to operate at a pressure above 100 bar and was positioned upstream of the expansion to allow particle-based optical diagnostics such as particle image velocimetry and fluid thermometry using thermographic phosphors (Abram et al. 2018).

The gas dynamics of the flow were characterised using a non-simultaneous combination of Toppler Schlieren and kHz-rate PIV. In the Schlieren measurements carried out for various pressure ratios up to 120, the location of the Mach disk was found at distances only slightly larger (\sim 3%) than the Crist correlation. The quasi-instantaneous Schlieren measurements revealed rapidly evolving fluctuations in the Mach disk location. The Mie scattering images obtained indicated a much higher light intensity in the supersonic region upstream of the Mach disk than could be caused by seeding particles alone. By comparing the present results with the previous studies on the onset of nucleation for argon at low temperatures, and based on some gas dynamics theoretical calculations, the most likely cause for the bright regions was the formation of a condensed phase. The Mie scattering image showed an extreme gradient at the location of the Mach disk, allowing its accurate description without the line-of-sight averaging effects of the Schlieren measurement. The location of the Mach disk was thereby sampled with a mean value which is in close agreement with that derived from the Schlieren measurements but with a larger standard deviation.

Particle image velocimetry was performed at 3 kHz, and the first and the second moment statistics could be obtained based on large sample sizes before the deposition of the seed particles on windows became critical. This sampling rate was too low to obtain temporally correlated data. PIV was applied in three regions of the flow, with the mean flow field revealing a jet spread half angle of 4.8° and a large recirculation zone expanding up to 3–4 channel heights (i.e. 150–200 mm) from the throat exit. A strong deceleration in the mean centreline velocity was observed in the “impingement” region, 2–3 channel heights from the throat exit, associated with a narrowing of the recirculation zone. At a distance of 250 mm downstream of the throat exit, a mostly uniform mean flow was observed. Single shots in the impingement section revealed a high degree of intermittency. Second moment and Reynolds stresses $\overline{v'_x v'_y}$ were derived from those single-shot data. The second moment of the axial velocity has a peak at 90 m/s in the near throat region and 55 m/s in the impingement region (the later corresponds to turbulence intensities over 30%). The peak Reynolds stresses in the shear layer were found to be about 800 m²/s² in the impingement region, and over 1000 m²/s² in the near throat region. A slight asymmetry was also observed in all profiles. Histograms were also presented for three locations near the top wall, and three locations near the centerline, all in the impingement region and each drawn from 3000 samples. They showed that on the centerline, the velocity probability density function (pdf) evolved from an asymmetrical profile with a longer wing towards the lower velocities to a symmetrical profile from $x = 115$ mm to $x = 160$ mm. In contrast with the results on the centerline, the distributions observed near the wall are normal-like.

To evaluate the relevance of these experimental data in a quantitative comparison with numerical simulations, a sensitivity analysis was performed, as well as a quantification of the uncertainty based on the PIV correlation statistics. A periscope was used for some of the measurements to propagate the beam from the channel exit and to avoid strong wall signals. The periscope was shown to have a negligible influence on the first and second order statistics when measuring in the impingement region but there seemed to be an effect when measuring in the near throat

region. The shorter distance between the exit of the test section and the periscope location possibly caused a disturbance in the near-throat flow measurements. Overall the measurements in the middle region (impingement region) can be quantitatively compared with numerical simulations, with a total uncertainty of 10 m/s ($\sim 5\%$) in the mean, 5 m/s ($\sim 8\%$) in the RMS velocity for the axial component and $380 \text{ m}^2/\text{s}^2$ ($\sim 30\%$) in the Reynolds stresses. The uncertainty in the near throat region is higher, namely 50 m/s in the mean velocity, 12 m/s in the RMS velocity and of $1000 \text{ m}^2/\text{s}^2$ in the Reynolds stresses.

The quantities as obtained in these experiments, such as the Mach disk distance and fluctuations, the mean flow velocity, the rms velocity and the Reynolds stresses, can be used for the validations of the results obtained with a Large Eddy Simulation (LES), taking into account compressible real gas effects. Additional insight can be gained using the experimental data for the comparison of the spatial scales of the instantaneous fields, or the shape of the probability density functions (pdf) of the turbulent fluctuations.

This study exemplifies the wealth of information derived from laser imaging techniques that gives insight into complex flow behaviour and that enables to improve predictive methods.

Acknowledgements The authors are grateful to Paul Bruce (Imperial College London) for discussion on the implementation of the Schlieren measurements, and to Christopher Abram (Universität Magdeburg, currently at Princeton University) for his support in implementing the high speed PIV system.

References

- Abram C, Fond B, Heyes AL, Beyrau F (2013) High-speed planar thermometry and velocimetry using thermographic phosphor particles. *Appl Phys B Lasers O* 111:155–160. <https://doi.org/10.1007/s00340-013-5411-8>
- Abram C, Fond B, Beyrau F (2015) High-precision flow temperature imaging using ZnO thermographic phosphor tracer particles. *Opt Express* 23:19453–19468. <https://doi.org/10.1364/OE.23.019453>
- Abram C, Fond B, Beyrau F (2018) Temperature measurement techniques for gas and liquid flows using thermographic phosphor tracer particles. *Prog Energy Combust Sci* 64:93–156. <https://doi.org/10.1016/j.pecs.2017.09.001>
- Arun Kumar R, Rajesh G (2017) Shock transformation and hysteresis in underexpanded confined jets. *J Fluid Mech* 823:538–561. <https://doi.org/10.1017/jfm.2017.231>
- Baughn JW, Hoffman MA, Takahashi RK, Launder BE (1984) Local heat transfer downstream of an abrupt expansion in a circular channel with constant wall heat flux. *J Heat Transf* 106:131–136. <https://doi.org/10.1115/1.3246753>
- Baab S, Lamanna G, Weigand B (2018) Two-phase disintegration of high-pressure retrograde fluid jets at near-critical injection temperature discharged into a subcritical pressure atmosphere. *Int J Multiph Flow* 107:116–130. <https://doi.org/10.1016/j.ijmultiphaseflow.2018.04.021>
- Burns RA, Danehy PM (2017) Unseeded velocity measurements around a transonic airfoil using femtosecond laser tagging. *AIAA J* 55(12):4142–4154. <https://doi.org/10.2514/1.J056154>
- Chauveau C, Davidenko DM, Sarh B, Gökalp I, Avrashkov V, Fabre C (2006) PIV measurements in an underexpanded hot free jet. In: 13th international symposium on the application of laser and imaging techniques to fluid mechanics, Lisbon, Portugal, 26–29 June
- Chuech SG, Lai M-C, Faeth GM (1989) Structure of turbulent sonic underexpanded free jets. *AIAA J* 27(5):549–559. <https://doi.org/10.2514/3.10145>
- Clancy PS, Samimy MO (1997) Two-component planar doppler velocimetry in high speed flows. *AIAA J* 35(11):1729–1738. <https://doi.org/10.2514/2.42>
- Crist S, Glass DR, Sherman PM (1966) Study of the highly underexpanded sonic jet. *AIAA J* 4(1):68–71. <https://doi.org/10.2514/3.3386>
- Dawson DM, Books BJ (1999) The Esso Longford gas plant accident—report of the Longford Royal Commission, Tech. rep. <https://www.parliament.vic.gov.au/papers/govpub/VPARL1998-99No61.pdf>
- DeLuca NJ, Miles RB, Jiang N, Kulatilaka WD, Patnaik AK, Gord JR (2017) Fleet velocimetry for combustion and flow diagnostics. *Appl Opt* 56(31):8632–8638. <https://doi.org/10.1364/AO.56.008632>
- Forkey JN, Finkelstein ND, Lempert WR, Miles RB (1996) Demonstration and characterization of filtered Rayleigh scattering for planar velocity measurements. *AIAA J* 34(3):442–448. <https://doi.org/10.2514/3.13087>
- Förster FJ, Baab S, Steinhausen C, Lamanna G, Ewart P, Weigand B (2018) Mixing characterization of highly underexpanded fluid jets with real gas expansion. *Exp Fluids* 59(3):44. <https://doi.org/10.1007/s00348-018-2488-1>
- Hwang C, Chow WL, Moslemian D (1993) Base pressure of a sudden expansion from a conical converging nozzle. *AIAA J* 31(4):657–662. <https://doi.org/10.2514/3.11600>
- Koppenwallner G, Dankert C (1987) Homogeneous condensation in N₂, Ar, and H₂O free jets. *J Phys Chem* 91:2482–2486. <https://doi.org/10.1021/j100294a008>
- Krall KM, Sparrow EM (1966) Turbulent heat transfer in the separated, reattached, and redevelopment regions of a circular tube. *J Heat Transf* 88:131–136. <https://doi.org/10.1115/1.3691456>
- Hahn DW, Necati Özisik M (2012) Heat conduction, 3rd edn. Wiley, Hoboken
- Lijo V, Kim HD, Setoguchi T (2012) Numerical investigation of the effects of base size on supersonic flow through a sudden duct enlargement. *Proc Inst Mech Eng Part G J Aerosp Eng* 226(12):1562–1572. <https://doi.org/10.1177/0954410011424984>
- Matthew MW, Steinwandel J (1983) An experimental study of argon condensation in cryogenic shock tubes. *J Aerosol Sci* 14(6):755–763. [https://doi.org/10.1016/0021-8502\(83\)90059-9](https://doi.org/10.1016/0021-8502(83)90059-9)
- McMillin BK, Palmer JL, Hanson RK (1993) Temporally resolved, two-line fluorescence imaging of NO temperature in a transverse jet in a supersonic cross flow. *Appl Opt* 32:7532–7545. <https://doi.org/10.1364/AO.32.007532>
- Meier GEA, Grabitz G, Jungowski WM, Witczak KJ, Anderson JS (1980) Oscillations of the supersonic flow downstream of an abrupt increase in duct cross section. *AIAA J* 18:394–395. <https://doi.org/10.2514/3.50770>
- Melling A (1997) Tracer particles and seeding for particle image velocimetry. *Meas Sci Technol* 8:1406–1416. <https://doi.org/10.1088/0957-0233/8/12/005>
- Michael JB, Edwards MR, Dogariu A, Miles RB (2011) Femtosecond laser electronic excitation tagging for quantitative

- velocity imaging in air. *Appl Opt* 50(26):5158–5162. <https://doi.org/10.1364/AO.50.005158>
- Miles RB, Connors JJ, Markovitz EC, Howard PJ, Roth GJ (1989) Instantaneous profiles and turbulence statistics of supersonic free shear layers by Raman excitation plus laser-induced electronic fluorescence (relief) velocity tagging of oxygen. *Exp Fluids* 8(1):17–24. <https://doi.org/10.1007/BF00203060>
- Naik SV, Kulatilaka WD, Venkatesan KK, Lucht RP (2009) Pressure, temperature and velocity measurements in underexpanded free jets using laser-induced fluorescence. *AIAA J* 47:839–849. <https://doi.org/10.2514/1.37343>
- Paul PH, Lee MP, Hanson RK (1989) Molecular velocity imaging of supersonic flows using pulsed planar laser-induced fluorescence of NO. *Opt Lett* 14(9):417–419. <https://doi.org/10.1364/OL.14.000417>
- Pfadler S, Dinkelacker F, Beyrau F, Leipertz A (2009) High resolution dual-plane stereo-PIV for validation of subgrid scale models in large-eddy simulations of turbulent premixed flames. *Combust Flame* 156(8):1552–1564. <https://doi.org/10.1016/j.combustflame.2009.02.010>
- Raffel M, Willert CE, Wereley ST, Kompenhans J (2007) Particle image velocimetry: a practical guide. Springer, Berlin
- Ragni D, Schrijer F, Oudheusden BW, Scarano F (2011) Particle tracer response across shocks measured by PIV. *Exp Fluids* 50:53–64. <https://doi.org/10.1007/s00348-010-0892-2>
- Rahimi M, Owen I, Mistry J (2003) Heat transfer between an under-expanded jet and a cylindrical surface. *Int J Heat Mass Transf* 46(17):3135–3142. [https://doi.org/10.1016/S0017-9310\(03\)00116-9](https://doi.org/10.1016/S0017-9310(03)00116-9)
- Scarano F (2013) Tomographic PIV: principles and practice. *Meas Sci Technol* 24(1):012001. <https://doi.org/10.1088/0957-0233/24/1/012001>
- Schreivogel P, Abram C, Fond B, Straußwald M, Beyrau F, Pfitzner M (2016) Simultaneous kHz-rate temperature and velocity field measurements in the flow emanating from angled and trenced film cooling holes. *Int J Heat Mass Transf* 103:390–400. <https://doi.org/10.1016/j.ijheatmasstransfer.2016.06.092>
- Sciacchitano A, Neal DR, Smith BL, Warner SO, Vlachos PP, Wieneke B, Scarano F (2015) Collaborative framework for PIV uncertainty quantification: comparative assessment of methods. *Meas Sci Technol* 26(7):074004. <https://doi.org/10.1088/0957-0233/26/7/074004>
- Sinha S, Bhabhe A, Laksmono H, Wölk J, Strey R, Wyslouzil B (2010) Argon nucleation in a cryogenic supersonic nozzle. *J Chem Phys* 132(6):064304. <https://doi.org/10.1063/1.3299273>
- Vinze R, Chandel S, Limaye MD, Prabhu SV (2017) Heat transfer distribution and shadowgraph study for impinging underexpanded jets. *Appl Therm Eng* 115:41–52. <https://doi.org/10.1016/j.applthermaleng.2016.12.046>
- Wieneke B (2015) PIV uncertainty quantification from correlation statistics. *Meas Sci Technol* 26(7):074002. <https://doi.org/10.1088/0957-0233/26/7/074002>
- Wilkes Inman J, Danehy P, Nowak R, Alderfer D (2008) Fluorescence imaging study of impinging underexpanded jets. In: 46th AIAA aerospace sciences meeting and exhibit. Reno, Nevada, 7–10 Jan 2008. <https://doi.org/10.2514/6.2008-619>
- Xiao C-N, Fond B, Beyrau F, T'Joen C, Henkes R, Veenstra P, van Wachem BGM (2018) Numerical and experimental investigation of the gas dynamics in a highly underexpanded confined real gas jet. *Flow Turbul Combust* (**submitted**)
- Yüceil KB (2017) A comparison of PIV and interferometric Rayleigh scattering measurements in the near field of underexpanded sonic jets. *Aerosp Sci Technol* 67:31–40. <https://doi.org/10.1016/j.ast.2017.03.034>
- Yu J, Vuorinen V, Kaario O, Sarjovaara T, Larimi M (2013) Visualization and analysis of the characteristics of transitional under-expanded jets. *Int J Heat Fluid Flow* 44:140–154. <https://doi.org/10.1016/j.ijheatfluidflow.2013.05.015>

Publisher's Note Springer Nature remains neutral with regard to jurisdictional claims in published maps and institutional affiliations.

Affiliations

Benoît Fond¹  · Cheng-Nian Xiao² · Christophe T'Joen³ · Ruud Henkes³ · Peter Veenstra³ · Berend G. M. van Wachem¹ · Frank Beyrau¹

✉ Benoît Fond
benoit.fond@ovgu.de

¹ Faculty of Process and Systems Engineering, Otto-von-Guericke-Universität Magdeburg, Magdeburg, Germany

² Department of Mechanical Engineering, Imperial College London, London, UK

³ Shell Global Solutions, Amsterdam, The Netherlands